

The turbulence driving parameter of molecular clouds in disc galaxies

Bastian Körtgen

Hamburger Sternwarte, Universität Hamburg, Gojenbergsweg 112, D-21029 Hamburg, Germany

Released 2020

ABSTRACT

Supersonic turbulence plays a pivotal role during the formation of molecular clouds and stars in galaxies. However, little is known about how the fraction of compressive and solenoidal modes in the velocity field evolves over time and how it depends on properties of the molecular cloud or the galactic environment. In this work, we carry out magnetohydrodynamical simulations of disc galaxies and study the time evolution of the turbulence driving parameter for an ensemble of clouds. We find that the time-averaged turbulence driving parameter is insensitive to the position of the cloud within the galaxy. The ensemble-averaged driving parameter is found to be rather compressive with $b \sim 0.5 - 0.7$, indicating almost time-independent global star formation properties. However, each individual cloud shows a highly fluctuating driving parameter, which would strongly affect the cloud’s star formation rate. We find that the mode of turbulence driving can rapidly change within only a few Myr, both from solenoidal to compressive and vice versa. We attribute these changes to cloud collisions and to tidal interactions with clouds or overdensities in the environment. Last, we find no significant differences in the average driving parameter between hydrodynamic and initially strongly magnetised galaxies. However, the magnetic field tends to reduce the overall fluctuation of the driving parameter. The average driving as well as its uncertainty are seen to be in agreement with recent constraints on the turbulence driving mode for solar neighbourhood clouds.

Key words: galaxies: ISM; ISM: kinematics and dynamics; ISM: magnetic fields; ISM: clouds; stars: formation

1 INTRODUCTION

Stars are born within self-gravitating, magnetised and turbulent molecular clouds. The complex dynamical interplay between gravity, turbulence, magnetic fields and (at more evolved stages) stellar feedback strongly shapes the density distribution of the parental cloud and thus determines the rate and efficiency at which stars form (Mac Low & Klessen 2004; Elmegreen & Scalo 2004; Scalo & Elmegreen 2004; Federrath & Klessen 2012). For supersonically turbulent, isothermal (and magnetised) gas the density probability distribution function (PDF) resembles a lognormal distribution, which means that the logarithm of the density (contrast) is Gaussian distributed (Vázquez-Semadeni 1994; Passot & Vázquez-Semadeni 1998; Federrath et al. 2008). However, the interstellar medium (ISM) of galaxies is a multiphase gas, strongly influenced by gravitational forces. Hence, the density PDF will take several forms that indicate, which physical process is dominant or at least relevant (Kainulainen et al. 2009; Ballesteros-Paredes et al. 2011; Schneider et al. 2015). For a thermally bistable gas, the den-

sity PDF becomes double-peaked. Each peak corresponds to a single thermal phase of the gas, and each phase can be fitted by a lognormal distribution (Seifried et al. 2011). When the gas has become sufficiently dense, gravity starts to become dominant. The subsequent flow of gas towards smaller scales and the resultant formation of power-law density profiles induces the formation of a power-law tail in the density PDF at high densities (Kritsuk et al. 2011). Over time, the transition point from the log-normal to the power-law part in the PDF will shift towards lower densities, as gravity starts to impact the more diffuse gas in the cloud (Burkhart et al. 2017). In addition, the power-law tail flattens with increasing star formation activity of the cloud (Federrath & Klessen 2013). However, in case the bistable gas is subjected to stellar feedback or strong turbulent phase mixing, a power-law tail can also form in a non-gravitating medium, thereby complicating the interpretation of the density PDF (Seifried et al. 2011; Tremblin et al. 2014).

An essential ingredient for current theoretical models of star formation, based on turbulent fragmentation of the gas, is

the width of the density distribution (Krumholz & McKee 2005; Padoan & Nordlund 2011; Hennebelle & Chabrier 2011; Federrath & Klessen 2012; Zamora-Avilés et al. 2012; Konstandin et al. 2016; Völschow et al. 2017). Theoretical studies have shown that there exists a relation between the variance of the density PDF and gas-dynamical quantities, such as the turbulent Mach number, \mathcal{M} , the ratio of thermal to magnetic pressure, β and the fraction of compressive or solenoidal modes in the turbulent velocity field, typically denoted by b . For a fully compressive driving of the turbulent field $b = 1$, whereas purely solenoidal driving implies $b = 1/3$ (see Federrath et al. 2010, for a first detailed investigation). Therefore, the gas dynamics, which affect the density variance, implicitly affect the star formation properties of the cloud. For example, Federrath & Klessen (2012) have shown that the star formation rate of a turbulent molecular cloud with equal Mach number is increased by a factor of $\gtrsim 10$, when the turbulent velocity field is changed from solenoidal to compressive.

Rather than treating the driving parameter, b , as an input parameter, several recent studies focused on retrieving it from the self-consistent gas dynamics in the analysed environment (Körtgen et al. 2017; Jin et al. 2017; Menon et al. 2020). While Körtgen et al. (2017) and Jin et al. (2017) find b to vary between $b \sim 0.3$ and $b \sim 0.8$ in their different simulations of molecular cloud formation, the study by Menon et al. (2020) finds a rather stable $b \sim 0.76$ in a simulated region, which is affected by radiative feedback. Furthermore, Pan et al. (2016) argue that supernova feedback induces mostly solenoidal motions due to the onset of the baroclinic instability in the post-shock region of the supernova remnant. These results all emphasise the impact of the various feedback mechanisms and involved physics on the turbulent velocity field.

Deriving the turbulence driving parameter from observations of molecular clouds is even more challenging. This is mostly due to the restriction of the data to at most two dimensions. However, it is nevertheless useful and necessary to confront theory with reality. For molecular clouds in the solar neighbourhood, Ginsburg et al. (2013) derived a lower limit of $b \sim 0.4$. Orkisz et al. (2017) analysed the solenoidal fraction of the velocity field in the Orion B cloud and showed that the fraction varies both as a function of position across the complex and radial distance to a given center (e.g. the position of the peak density). In terms of the driving parameter, this latter study deduced that b varies from $b > 0.3$ to $b \lesssim 1$, i.e. the gas motion is neither fully solenoidal nor entirely compressive. Their most likely value was about $b \sim 0.4$, which indicates equipartition between the two modes (Federrath et al. 2010). Kainulainen & Federrath (2017) studied a set of 13 solar neighbourhood clouds and argued that $b \in [0.4, 0.7]$ provides a strict range of values. As these authors point out, the driving parameter was derived from the density variance - Mach number relation, despite the fact that their data did not necessarily follow such a relation. In contrast to clouds in the solar neighbourhood, the Galactic center may provide a significantly different environment. As Federrath et al. (2016) show in their study of the central molecular zone cloud G0.253+0.016, the driving of turbulence in this region might be almost fully solenoidal with $b \sim 0.22 \pm 0.12$ due to the increased shear. Hence, understanding the driving of turbulence in different environ-

ments of the Galaxy and within molecular clouds is crucial for the understanding of the local gas dynamics and the subsequent star formation process.

This work strives to add further insights into the driving of turbulence by analysing the time evolution of the turbulence driving parameter in a set of molecular clouds formed in disc galaxies. The study is structured as follows: In Sect. 2 we briefly discuss the used numerical tools and initial conditions. Sect. 3 discusses the findings of this study, before it is closed with a summary in Sect. 4.

2 NUMERICAL METHOD AND INITIAL CONDITIONS

2.1 Methods

We use the finite volume code FLASH (version 4.2.2, Dubey et al. 2008). The equations of ideal magnetohydrodynamics are solved each timestep on the numerical grid with a five-wave Riemann solver (Bouchut et al. 2009; Waagan et al. 2011). To ensure the solenoidal constraint of the magnetic field, we use a hyperbolic cleaning scheme (Dedner et al. 2002). Poisson's equation for the self-gravity of the gas is solved with a Barnes-Hut tree solver (see e.g. Lukat & Banerjee 2016, for a GPU version). The thermodynamic evolution of the gas is treated by optically thin heating and cooling, where we follow the approach by Koyama & Inutsuka (2002, with modifications by Vázquez-Semadeni et al. (2007)), i.e. the heating rate is constant and the temperature-dependent cooling rate is provided in tabulated form.

The cubic simulation domain has an edge length of $L = 40$ kpc and the root grid is at a grid resolution of $\Delta x_{\text{root}} = 625$ pc. Over the course of the evolution, the grid is adaptively refined (Berger & Olinger 1984) once the local Jeans length is resolved with less than 32 grid cells (as recommended based on the results in Federrath et al. 2011). De-refinement is initiated when the Jeans length instead is resolved by more than 64 grid cells. In total, we allow for a maximum of 11 refinement levels, which gives a peak spatial resolution of $\Delta x_{\text{peak}} = 19.5$ pc. The gas scale height is thus resolved with $\gtrsim 10 - 15$ grid cells in the major part of the disc (Körtgen et al. 2019). Any fragmentation at later times from $R \sim 4 - 5$ kpc on can thus assumed to be physical (see also Truelove et al. 1997). To extract gas dynamics within the formed clouds solely driven by gravity, neither stellar feedback nor sink particles are included in the current study and we introduce an artificial pressure term on the highest level of refinement.

2.2 Initial Conditions

An in depth description of the initial conditions is given in Körtgen et al. (2019, see also Körtgen et al. (2018)), so we provide only a brief overview here.

We set up a thin disc, following the approach by Tasker & Tan (2009), with a radially increasing gas scale height. The gas density profile is adjusted in such way that the Toomre stability parameter is initially constant at $Q = 2$ in the major part of the disc. In the inner most part it is

set to $Q = 20$ to increase the stability of the less well resolved region. The final mass of the disc is $M_{\text{disc}} \approx 10^{10} M_{\odot}$, similar to the mass of the LMC. We use a fixed external logarithmic gravitational potential to account for the effect of dark matter and old stars, which also provides a flat rotation curve. The majority of the performed simulations starts with a purely toroidal magnetic field, where the field strength is coupled to the gas density, i.e. $B \propto \rho^{1/2}$, which results in a constant ratio of thermal to magnetic pressure. We do not impose any turbulent perturbation in order to simplify the initial conditions. Hence, any local velocity fluctuations at later stages are the result of gravitational fragmentation and self-consistently generated dynamics (i.e. cloud-cloud interactions).

3 RESULTS

3.1 Global view in a nutshell

Fig. 1 presents column density maps of the hydrodynamic (top panels) and the magnetised (bottom) discs, separated in time by $\Delta t = 200$ Myr, which corresponds to almost an entire disc rotation at $R = 8$ kpc.

With time, the initially smooth density profile is distorted, because the discs fragment into individual overdensities. While the hydrodynamic disc breaks up into several rings due to the onset of the Toomre instability, the magnetised galaxy builds up filamentary structures, which extend into the radial and azimuthal directions. The latter fragmentation pattern is a consequence of the Parker instability as the dominant mode of fragmentation (Mouschovias et al. 2009; Körtgen et al. 2018, 2019). After one additional disc rotation the shape of the galaxies is markedly different. The hydrodynamic disc has broken up into many almost spherical objects. The magnetised galaxy shows more filamentary structures. Here, the magnetic field restricts the motion of the diffuse gas. Hence, gas is not arbitrarily absorbed by the formed clouds. We emphasise the presence of spiral features around some clouds in both galaxies due to the cloud's bulk rotation. At even later times, the global disc morphology looks very similar. This indicates that, at this stage, the magnetic field does not have a pronounced impact on the global dynamics of the disc. Filamentary structures are now also seen in the hydrodynamic galaxy as a consequence of cloud-cloud interactions.

In the top row of Fig. 2 we show the divergence of the velocity field at a time close to the end of the simulation for both discs (dark: diverging, bright: converging). While this operation on the residual velocity field generates filamentary structures, there still appear pronounced differences. For instance, the hydrodynamic galaxy reveals a much more converging velocity field throughout the disc. In contrast, the magnetised galaxy reveals large patches of diverging gas in between kpc-scale filaments with a primarily converging field. In addition, the hydrodynamic disc allows for the formation of small scale bundles in the divergence field (see e.g. the pattern near $x = +6$ kpc and $y = +2$ kpc), whose formation is suppressed in the magnetised galaxy.

In the bottom panel of Fig. 2, we show the vorticity. Here, again, filamentary structures can be identified. In contrast to the divergence field, these are not as thick, indicating that

the vorticity throughout the disc seems to show a quite common orientation. In general, regions of pronounced changes in the divergence or the vorticity correlate well with gas structures emerging from dynamical interactions, such as cloud-cloud collisions. However, both discs do not show any systematic trends e.g. with respect to the distance from the center of the galaxy.

3.2 Time evolution of cloud properties

In this section we focus on the time evolution of dynamical quantities of the found clouds. Before we commence, we describe the cloud tracking algorithm.

3.2.1 Method to track the clouds

At a given time, a domain of size $L_x \times L_y \times L_z = 20 \times 20 \times 2$ kpc³ centered on the galaxy is searched for connected regions. The regions are defined by a minimum density, $n_{\text{min}} = 100 \text{ cm}^{-3}$, which is about the average number density of molecular clouds in the Milky Way (Blitz et al. 2007; Dobbs et al. 2014). A grid cell belongs to a certain structure if its density is similar (provided some uncertainty) to the one of its nearest neighbours and further has a spatial connection to them. The search starts in the cell with the highest density. Once, all objects with $n_{\text{min,obj}} \geq n_{\text{min}}$ have been found, their current center of mass position and bulk velocity are used to follow their evolution in time. At the next timestep – we use $\Delta t = 2$ Myr –, a volume of $V = 1 \text{ kpc}^3$ centered on the predicted center of mass is searched for clouds and the cloud with its center of mass closest to the predicted one is chosen (see also Tasker & Tan 2009). We note here that, in the current version and as a difference to Tasker & Tan (2009) and Jin et al. (2017), the cloud tracking algorithm does not search for newly formed clouds and thus traces only the evolution of the firstly identified ensemble of clouds.

3.2.2 Comparing cloud dynamical properties

If not stated differently, the left panel in the following discussion corresponds to the hydrodynamic disc, while the right panel indicates results of the magnetised galaxy. In all figures, the grey lines indicate the evolution of each individual cloud, the red thick line is the cloud-mass weighted average, and the blue dashed lines represents the evolution of an example cloud¹.

In Fig. 3 we show the time evolution of the average number density of the clouds. The large difference in density between the two scenarios is initially due to the higher density of the magnetised galaxy, which is necessary to keep the Toomre parameter at $Q = 2$. Apart from this initial difference, the long term evolution of the cloud's average density is very similar. There appear, however, subtle variations, i.e. the magnetised clouds reach higher densities of up to $\langle n \rangle \sim 10^4 \text{ cm}^{-3}$, whereas there is only one cloud at a single time in the hydrodynamic disc, which reaches such high average densities. The *average* instead is less affected,

¹ To be more precise, it is the same cloud in all plots.

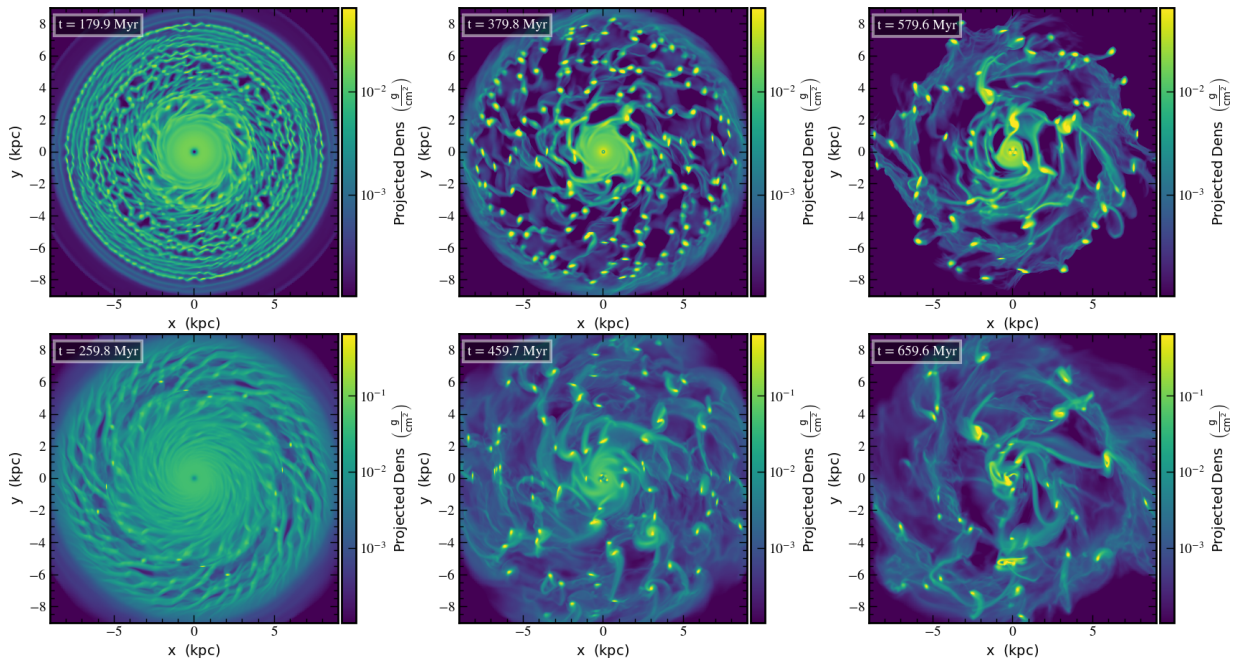


Figure 1. Surface density maps of the hydrodynamic (top) and magnetised disc (bottom) at three times, starting from the point where the first diffuse ($n_{\min} \geq 10 \text{ cm}^{-3}$) clouds have been identified. Note the different morphology of the fragmented disc and the increased density in the diffuse gas for the MHD disc at later times.

with a difference of about a factor of two. The overall time evolution of the average is more pronounced in the hydrodynamic disc and a plateau is reached after about 200 Myr of evolution (i.e. one disc rotation). As can be seen from the evolution of the example clouds, both ensembles are affected by cloud-cloud interactions with actual collisions resulting in a sudden increase of the average density². Interestingly, this effect is seen for almost every cloud. However, collisions/mergers induce only a temporarily limited increase in the average density and it takes several interactions for the cloud to become denser on average with time.

The time evolution of the velocity dispersion³ is shown in Fig. 4. As expected for unimpeded gravitational collapse, the velocity dispersion increases over time. The retrieved velocity dispersion evolves very similar in both galaxies, but is shifted to larger values in the MHD disc. The scatter, in contrast, is larger in the hydrodynamic case, which represents a larger variety of cloud properties. While it takes about one disc rotation to reach saturation in the magnetised disc, the hydrodynamic clouds still show a net increase over the course of about one and a half disc rotations and have not reached a saturated stage yet. Given the fact that the velocity dispersion is calculated from the size-linewidth relation $\sigma_v \sim 1.1R^p$, with $p = 0.38$ and R being the cloud-size (Larson 1981), the saturation indicates a phase in which the clouds do not grow anymore. The typical cloud temperature is about $T \sim 30 \text{ K}$, which corresponds to a sound speed

of about $c_s \sim 0.4 \text{ km/s}$. Therefore, sonic Mach numbers, as derived from Fig. 4, are in the range of $\mathcal{M}_s \sim 15 - 25$.

3.2.3 Additional dynamics of the magnetised clouds

Fig. 5 emphasises the time evolution of the cloud’s Alfvén Mach number and plasma- β . Similar to the sonic Mach number, the average Alfvén Mach number appears to reach saturation after one disc rotation. However, as inferred from the example cloud, individual clouds can show dramatic changes in the dynamic interplay of turbulence and magnetic fields. In general, all clouds are seen to be super-Alfvénic. This is also a result of matter accretion along the field lines, which results in a net decrease of the Alfvén speed when the field is not amplified sufficiently. Please note that the identified clouds start out trans- to slightly super-Alfvénic⁴ and reach values of $\mathcal{M}_A \gtrsim 3$ after $\sim 40 \text{ Myr}$. The ratio of thermal to magnetic pressure of the clouds varies between $\beta \sim 0.01 - 1$ for the majority of the clouds, with a rather stable average value of $\langle \beta \rangle \sim 0.2 - 0.4$, which is also in agreement with the constraints discussed by Kainulainen & Federrath (2017) for a set of solar neighbourhood clouds. Furthermore, the average value also fits the global disc average (Körtgen et al. 2019).

3.3 The density variance - Mach number relation

Having the time evolution of the relevant quantities at hand, one can investigate whether there emerges a relation between these and the density-variance. For the logarithmic

² We point out that the impact of the artificial pressure term, which results in an adiabatic behaviour in the innermost region of the core, does not affect the resulting (average) cloud radii and densities

³ Derived from a size-linewidth relation due to the limited numerical resolution and as a guideline for the internal dynamics.

⁴ We expect the initial conditions to be sub- to trans-Alfvénic for increasing resolution.

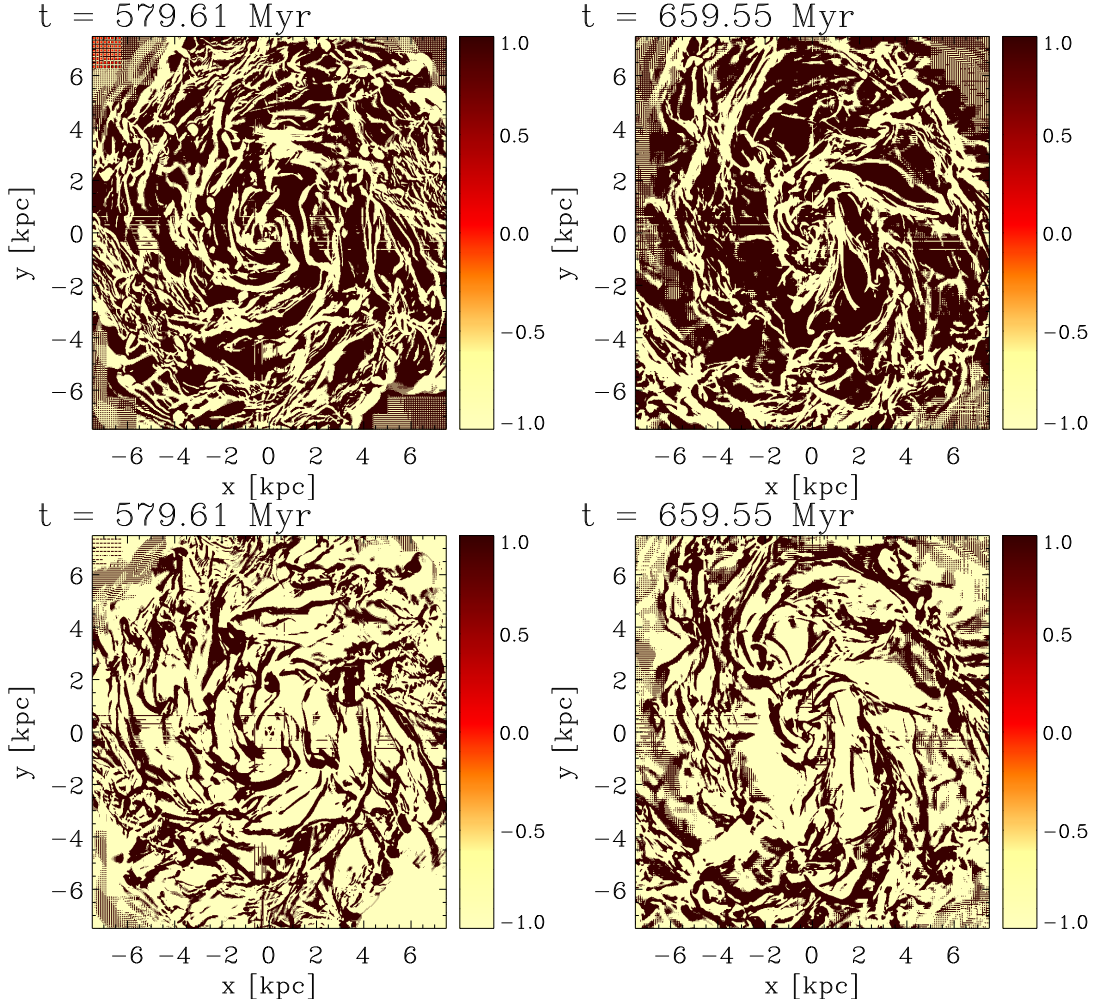


Figure 2. *Top:* Divergence of the projected residual (rotation curve subtracted) velocity field for the hydrodynamic (left) and magnetised (right) discs shortly before the end of the simulation. Both discs reveal filamentary structures of the divergence field. However, there appear more converging regions in the hydrodynamic disc. Note the large patches of diverging gas in the MHD disc. *Bottom:* Vorticity. The colour bar is arranged that converging regions are shown in bright colour, while diverging regions are shown as the dark patches. In the bottom panel, the same colour coding holds for negative and positive vorticity.

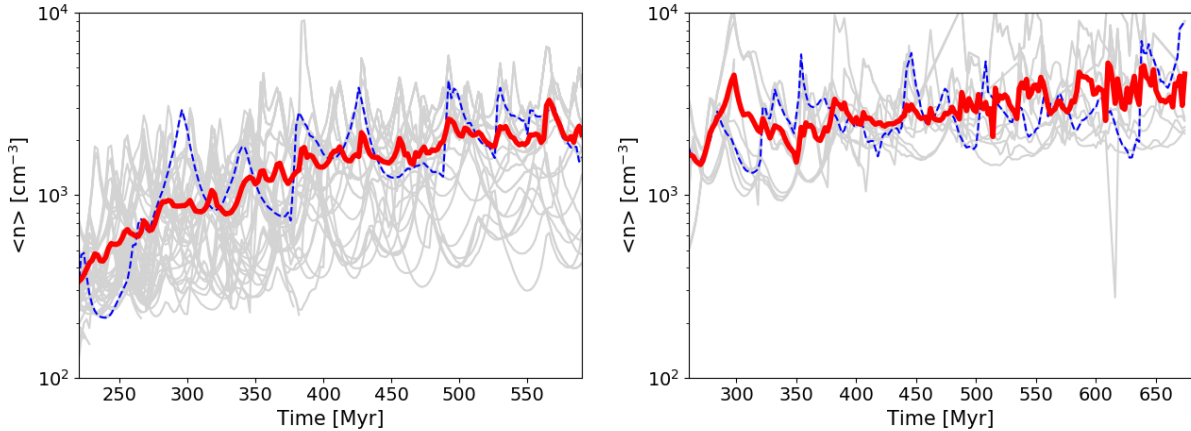


Figure 3. Average number density of the tracked molecular clouds as a function of time. In grey we show the evolution of each individual cloud, while the thick red line denotes the average over all clouds. The blue dashed lined highlights the evolution of a single cloud. Left for the hydrodynamic case. Right for the magnetised case.

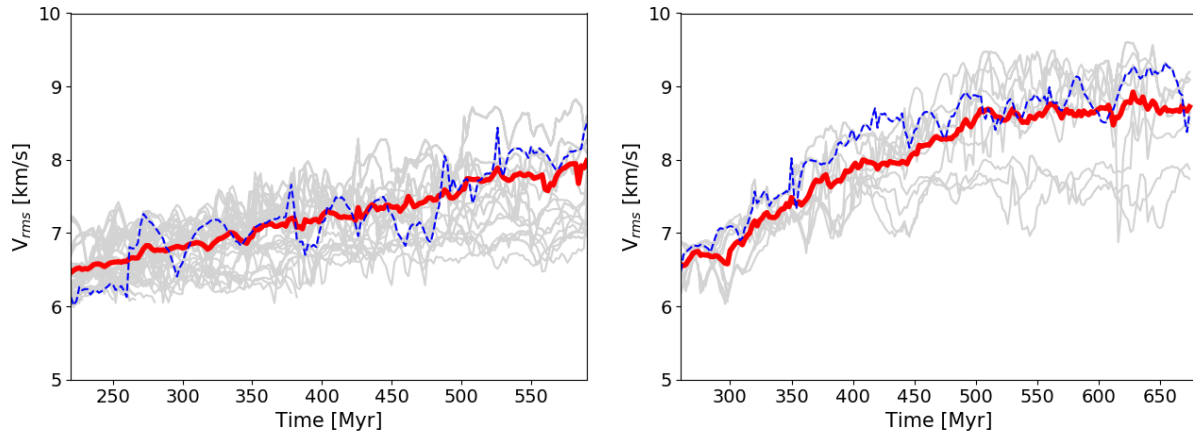


Figure 4. Velocity dispersion of the tracked molecular clouds as a function of time. In grey we show the evolution of each individual cloud, while the thick red line denotes the average over all clouds. The blue dashed lined highlights the evolution of a single cloud. Left for the hydrodynamic case; right for the magnetised case.

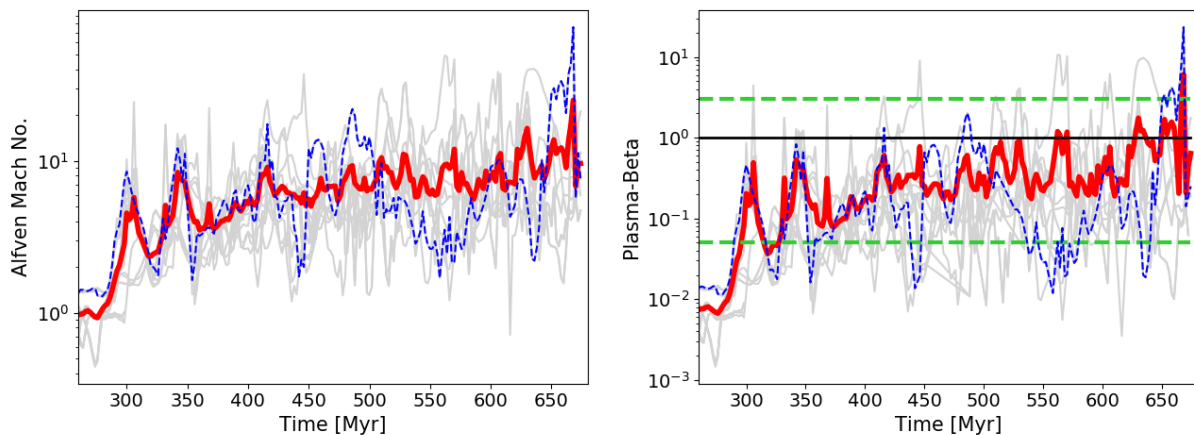


Figure 5. *Left:* Alfvén Mach number of the tracked molecular clouds as a function of time. *Right:* Plasma- β as a function of time. The line colors and styles have the usual meaning. In the right sub-figure, the black line denotes $\beta = 1$ and the green dashed lines indicate upper and lower limits for the magnetisation of solar neighbourhood clouds as constrained in Kainulainen & Federrath (2017).

density contrast this relation is given by (e.g Federrath & Klessen 2012, and references therein)

$$\sigma_{\ln(\rho/\rho_0)}^2 = \ln \left(1 + b^2 \mathcal{M}^2 \frac{\beta}{\beta + 1} \right). \quad (1)$$

We stress here that we remove systematic motions in the velocity field of the cloud and correct for a gradient in density, which would affect the density variance (Federrath et al. 2011). Fig. 6 shows the resulting density variance - Mach number relation for the hydrodynamic and magnetised discs. We show all ensemble clouds at all times, where the time is colour coded. As is observed, a relation emerges in the hydrodynamic case, which is, however, not described by eq. 1. At first, the density variance is too low for the estimated Mach numbers and, secondly, the relation appears rather linear than logarithmic. Interestingly, in the magnetised counterpart, a logarithmic relation is slightly recognised, which indicates that the overall relation is changed quite significantly by the magnetic field. The spread across the clouds is larger, but the overall density variances come closer to the theoretical values. However, for individual snapshots in

time, no significant correlation would be observed. This is especially clear for the MHD disc, where the majority of data points at late times (yellow) show a rather flat distribution, while the hydrodynamic clouds set up a point cloud between $\mathcal{M}^2 \sim 10^4 - 10^5$ without any clear trend. In any case, in both discs the derived driving parameters would be far too low. This has recently been discussed in Jin et al. (2017). The authors showed that the derived b is only a lower limit and it was seen to increase with increasing numerical resolution. We stress here that also no correct relation emerges, when using the velocity dispersion from the size-linewidth relation.

3.4 The turbulence driving parameter derived from the compressive ratio

Since Fig. 6 indicates the lack of a relation between the density variance and Mach number as provided by analytical models of turbulent fragmentation (Molina et al. 2012), we refrain from using this relation. We show in the appendix

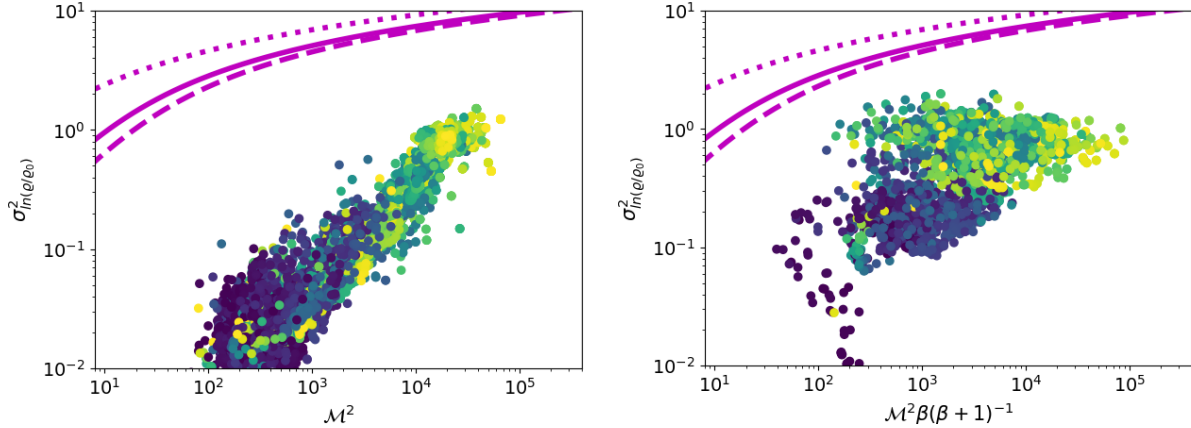


Figure 6. Density variance – Mach number relation at different times (blue: early, yellow: late). In the right panel, we show the magnetised version, which accounts for the plasma- β . Although the magnetised disc is closer to the theoretical prediction, no relation between the density variance and the Mach number term arises. In contrast, a clear relation is seen in the hydrodynamic case. However, the non-converged velocity field and the resulting inaccurate Mach numbers yield a relation that is far off the theoretical ones (purple lines). Dotted: $b = 1$, solid: $b = 0.4$, dashed: $b = 1/3$.

below that the density PDFs are dominated by a power-law tail. Hence, the application of the log-normal density variance should be taken with caution. However, using instead the density variance for the linear density contrast, ρ/ρ_0 ,

$$\sigma_{\rho/\rho_0}^2 = b^2 \mathcal{M}^2 \frac{\beta}{\beta + 1} \quad (2)$$

gives b -values, which are still too low. We re-iterate that the reason for this discrepancy is the lack of numerical resolution in our simulations, as previously found in Jin et al. (2017). We thus concentrate in the following on the driving parameter as derived from the compressive ratio $\chi = \langle v_{\text{comp}}^2 \rangle / \langle v_{\text{sol}}^2 \rangle$, where v_{comp} and v_{sol} are the compressive and solenoidal components of the velocity field. These can be retrieved via a Helmholtz decomposition in Fourier space. It can then be shown (Pan et al. 2016) that the compressive ratio and the turbulence driving parameter are related via

$$b_\chi = \sqrt{\frac{\chi}{1 + \chi}}. \quad (3)$$

We point out that this relation provides only an approximation to the true value of b , which can be retrieved from equations 1 and 2. We further note here that we remove any systematic motion in the velocity field, i.e. bulk motions in spherical shells around the center of mass. Thus, the compressive ratio in this study is comparable to the turbulent compressive ratio given in Pan et al. (2016, see also (Jin et al. 2017; Mandal et al. 2020; Menon et al. 2020)).

The resulting time evolution of the cloud-mass weighted average driving parameter, as well as of its standard deviation, is provided in Fig. 7. Surprisingly, there is almost no pronounced difference between the hydrodynamic (left) and magnetised clouds (right). The magnetised driving parameter appears to be slightly higher, but is still around $b_\chi \sim 0.5^5$. A closer look at the early evolution reveals that the magnetised parameter starts fluctuating earlier, after

~ 100 Myr, while the hydrodynamic driving parameter keeps its initial value for over half a rotation of the galaxy (again estimated at $R = 8$ kpc). Over the course of the evolution, the average b_χ starts to fluctuate quite strongly, thereby taking values from fully solenoidal to strongly compressive. However, despite the large fluctuations, both average driving parameters are within the bounds estimated by Kainulainen & Federrath (2017, green dashed lines). Given the fact that we only include gravity here, the tendency towards compressive driving is not surprising. Please note that, as summarised in Federrath et al. (2017), stellar feedback is also likely to drive compressive turbulent motions.

The thin blue line underlines the time evolution of the driving parameter for an individual cloud. Here, large fluctuations and deviations from the average are evident. For example, the hydrodynamic example cloud shows a stage near $t \sim 370$ Myr, where its turbulence would be described as fully compressive. In contrast, not even 30 Myr later, around $t \sim 400$ Myr, its driving parameter has dropped to $b_\chi \sim 0.2$, which indicates purely solenoidal driving. Similar short-period variations are observed for the example cloud in the magnetised disc. Both example clouds furthermore show a long-periodic modulation, with the magnetised modulation being less clear. We point out that not all clouds show such clear modulation patterns. However, the short- and long-period features can be interpreted as local and global (i.e. galactic-scale) processes affecting the velocity field in the clouds.

Fig. 8 analyses the behaviour of the turbulence driving mode as a function of distance to the galactic center. The various lines denote time averages over a period of 50 Myr or over the full tracking period. Although the spatial distribution of clouds in the hydrodynamic disc is narrower, there is no difference to the magnetised ensemble of clouds. In addition, we do not find any systematic trends with position in the galaxy, although the large fluctuations hint towards small temporal variations, which could indicate a trend at the given time. Contrary to the missing radial trend, a few small differences can be recognised. Initially, the clouds in

⁵ Note that we use b_χ and b_{driv} interchangeably in the figures.

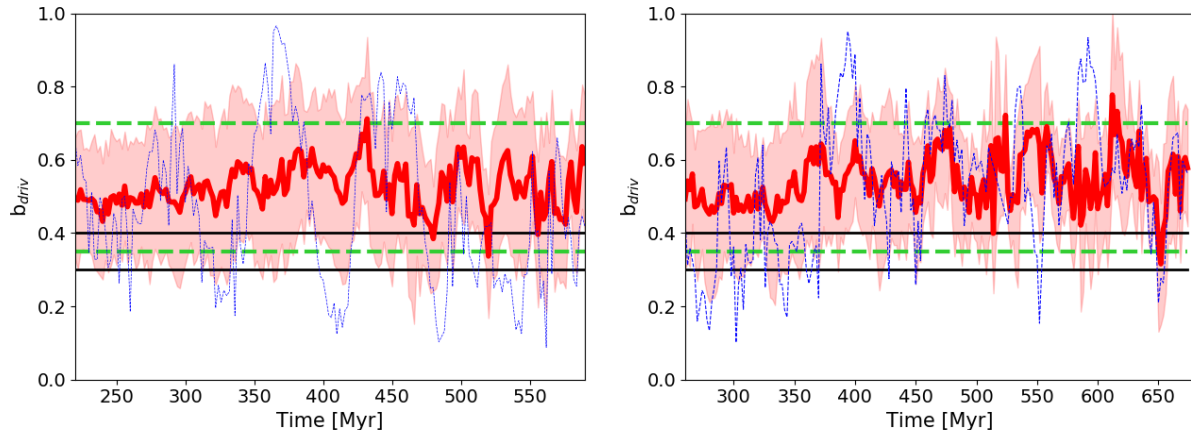


Figure 7. Turbulence driving parameter b as derived via the compression ratio χ as a function of time for the ensemble of clouds identified in the hydrodynamic (left) and MHD (right) disc. Although strong variations per cloud from purely solenoidal to largely compressive are seen, the mass-weighted average driving parameter is about $b \sim 0.5$, indicating slightly compressive driving. In blue we show the evolution of b for an exemplary cloud. There are times with little variation and events, where b changes dramatically within only a few Myr. The stronger fluctuations are due to cloud collisions and tidal interactions. The horizontal black lines denote natural ($b = 0.4$) and purely solenoidal driving ($b = 1/3$), while the green dashed lines highlight the possible upper/lower limit for solar neighbourhood clouds discussed in Kainulainen & Federrath (2017, i.e. $b_l = 0.35$ and $b_u = 0.7$).

the magnetised disc show a slightly lower driving parameter $0.4 < b \lesssim 0.5$, whereas the hydrodynamic clouds reveal $b \sim 0.55$. The fluctuations in b_χ are larger in the hydrodynamic ensemble, which was also recognised in Fig. 7. This implies that the magnetic field tends to (slightly) decrease the overall variation in b_χ .

3.4.1 What causes the changes in the driving parameter?

Keeping in mind the absence of stellar feedback, the lack of a correlation between the driving parameter and the position of the cloud in the galaxy seems to be in contradiction with recent estimates of the turbulence driving mode in Galactic molecular clouds, which show mixed to mildly compressive turbulence in the solar neighbourhood (Ginsburg et al. 2013; Kainulainen & Federrath 2017) and solenoidal forcing near the Galactic center (Federrath et al. 2016). Hence, there must be other mechanisms that induce the derived changes in the forcing over time. In Fig. 9 we show the time evolution of b_χ for the example cloud. We extract a certain interval of about 30 Myr and present surface density maps centered on the cloud’s center of mass. The sequence of maps clearly shows that the cloud undergoes a collision/merger with a different, slightly less dense object. The corresponding times shown in the surface density maps are highlighted as vertical lines in the time evolution of b_χ . The driving mode is initially compressive with $b_\chi \sim 0.6$. Interestingly, the appearance of the collider reduces the forcing parameter to $b_\chi \sim 0.2$. This implies that tidal forces induce shear across the cloud, given that the net tidal field is disruptive (see e.g. discussion in Jog 2013). The later stages, which resemble an in-spiral phase and the actual collision raise the value to $b_\chi \sim 0.8$. This is what should be expected from a collision. After the collision event, however, the driving parameter decreases again to solenoidal values. This is, because the collision was not head-on and thus increased the shear within the cloud. We point out that this change of b_χ from ~ 0.3 to ~ 0.8 and

back to solenoidal happens on timescales of less than 10 Myr (in agreement with the findings by Körtgen et al. 2017). Extrapolating this to all clouds, we conclude that the nature of the collision event is vital for the short-term temporal variation of the driving parameter.

3.4.2 Density dependence of the driving parameter

Finally, we briefly study the influence of the choice of the lower threshold density for the identification of overdense objects. Fig. 10 shows the time evolution of the average driving parameter of about 16 clouds. The left panel shows the standard threshold density of $n = 100 \text{ cm}^{-3}$. In the right panel we have increased the lower threshold by a factor of ten, thus corresponding to molecular clump or core densities. As expected, the driving mode becomes more compressive for the higher threshold density since this material is more tightly bound by gravity, although the increase can temporarily be rather small (see also Orkisz et al. 2017). The average driving parameter over this period is $b_{\text{cloud}} \pm \Delta b_{\text{cloud}} = 0.56 \pm 0.04$ for the fiducial threshold and $b_{\text{dense}} \pm \Delta b_{\text{dense}} = 0.62 \pm 0.07$ in case of the increased lower density bound. Please note the time evolution of the driving parameter for the example clouds. These nicely show that the driving mode can change significantly over the course of 25 Myr and also does not represent the ensemble well.

4 SUMMARY AND CONCLUSIONS

We present a study on the time evolution of an ensemble of clouds formed in disc galaxies. We focus on a hydrodynamic disc and a strongly magnetised disc with an initial plasma- $\beta = 0.25$. The clouds are identified shortly after the discs have fragmented on large scales either due to the classical Toomre or the Parker instability. We find that the dynamical quantities, relevant for the turbulent properties of the

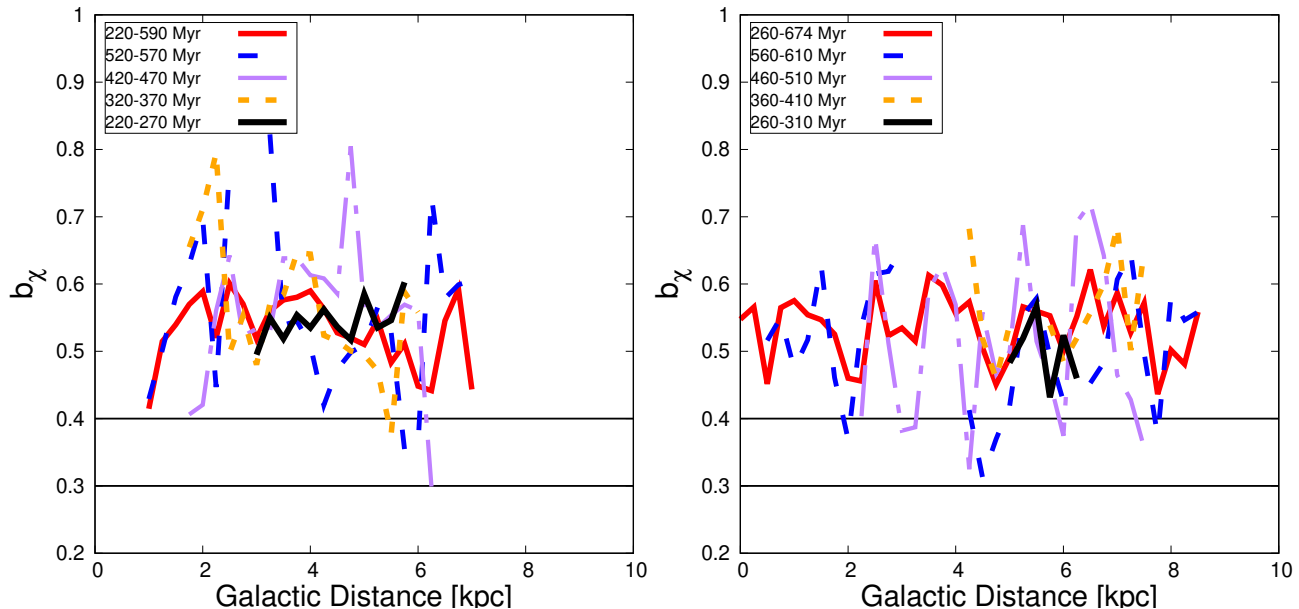


Figure 8. Turbulence driving parameter b as derived via the compressive ratio χ as a function of distance from the galactic center at various times and averaged over an interval of $\Delta t_{\text{av}} = 50$ Myr. Two facts are observed: 1) The driving parameter fluctuates less in the magnetised case and 2) it is generally slightly smaller than the corresponding hydrodynamic case. There is also only small variation in b over the course of a disc rotation. Note that the magnetised clouds are initially less compressive.

clouds, do not vary significantly when including a magnetic field. In a next step, we determined whether there arises a relation between the density variance and the turbulent sonic Mach number. Both galaxies show some kind of a relation. This, however, does not match the theoretical expectation for isothermal, turbulent gas, primarily because of the lack of numerical resolution in our simulations. As a consequence, we do not determine the driving parameter from the density variance - Mach number relation, but rather via the compressive ratio. Our main findings concerning the properties and evolution of the driving parameter obtained this way are:

- The derived driving parameter varies between fully solenoidal ($b_\chi \sim 1/3$) and entirely compressive ($b_\chi \sim 1$) driving.
- The *average* driving parameter, b_χ , does not significantly vary over the evolution of about ~ 400 Myr.
- In contrast, for individual clouds, we find large fluctuations as well as times of little to almost no variation.
- The largest fluctuations of b_χ can be associated with external distortions such as cloud-cloud mergers.
- Collisions between clouds induce a rapid change of b_χ within only a few Myr.
- The tidal forces exerted onto each cloud by its environment can reduce the driving parameter as they increase the shear.
- In our current framework, there appear no variations across the disc.
- Taking the magnetic field into account slightly reduces the spread/the uncertainty in b_χ .

We conclude that the merger history and/or the environment play a significant role in shaping the turbulent velocity field of molecular clouds in galaxies.

ACKNOWLEDGEMENT

BK thanks the anonymous referee for her/his comments, which helped to clarify the findings of this study. BK acknowledges Paris-Saclay University's Institut Pascal program "The Self-Organized Star Formation Process" and the Interstellar Institute for hosting discussions that nourished the development of the ideas behind this work. BK further acknowledges discussions with Robi Banerjee, Urs Schäfer, Wolfram Schmidt, Simon Selg and Pranjal Trivedi (in alphabetical order) and funding via the Australia-Germany Joint Research Cooperation Scheme (UA-DAAD) and from DFG grant BA3706/15-1. The simulations were run on HLRN-III under project grant hhp00043. The FLASH code was in part developed by the DOE-supported ASC/Alliance Center for Astrophysical Thermonuclear Flashes at the University of Chicago. Figs. 1 and 9 were generated with *GUFY*, a graphical user interface for the analysis of FLASH data with yt, developed by F. Balzer (University of Hamburg).

APPENDIX A: DENSITY PROBABILITY DISTRIBUTION FUNCTION

A way to study the dynamics of molecular clouds is by analysing their (column-) density distribution. The results are shown in Fig. A1 for different times. The PDF is almost flat at the earliest time, when the cloud has just formed via compression of gas flows due to the Parker instability. Over time, the PDF develops a power-law shape. At some times, a clear log-normal part is observed. In any case, it is clear that the PDF is more likely to be a power-law than a combination of lognormal and power-law, probably due to the lack of resolution. Hence, deriving the turbulence driving parameter from the logarithmic density variance - Mach number relation should be taken with caution.

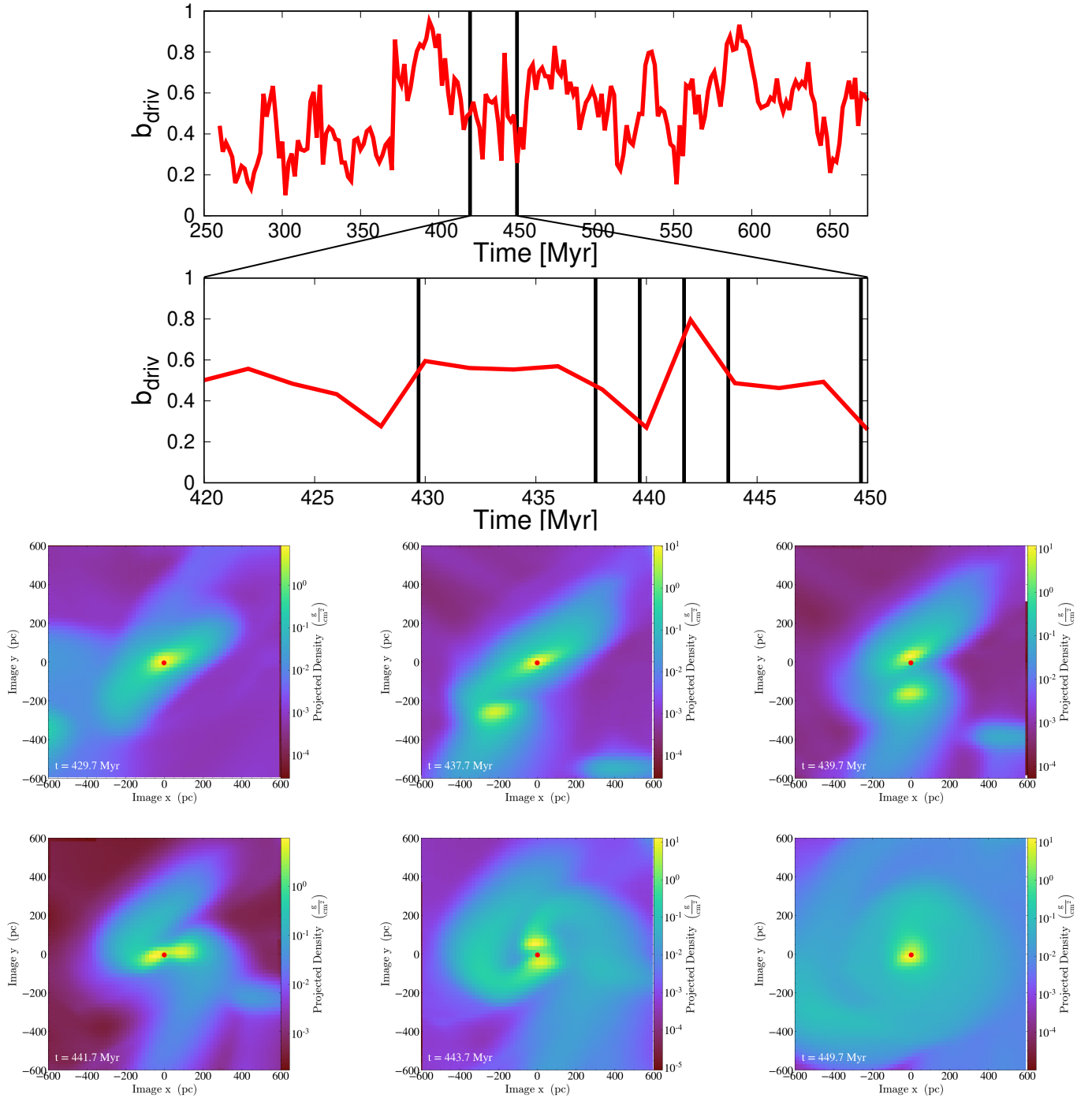


Figure 9. *Top two panels:* Time evolution of the turbulence driving parameter for the example cloud, where a specific time period is highlighted. *Bottom panels:* Surface density maps of a $1.2 \times 1.2 \text{ kpc}^2$ area centered on the cloud’s center of mass (indicated by the red dot). Each panel is highlighted by a vertical line in the time evolution plot (sequence: top to bottom and left to right). The sequence of maps shows a cloud merger and emphasise that this process initiates at first a *decrease* in the driving parameter due to tidal forces inducing shear. The first merger process is highly compressive with $b \sim 0.8$. Note the inspiral-phase after the closest approach, which results in strong shearing within the cloud and subsequently in low values of b .

APPENDIX B: RESOLUTION STUDY

In Fig. B1 we study the influence of the numerical resolution on the calculation of the average turbulence driving parameter, b_{driv} . As investigated in Jin et al. (2017, see also Körtgen et al. (2017)), *full* numerical convergence is

achieved only with sub-parsec resolution. We show two resolutions, namely our fiducial resolution with $\Delta x = 19.5 \text{ pc}$ and a slightly higher one with $\Delta x = 9.7 \text{ pc}$. The time axis is given in time relative to the time when clouds are identified for the first time, t_0 .

The driving parameter in the higher resolution run seems

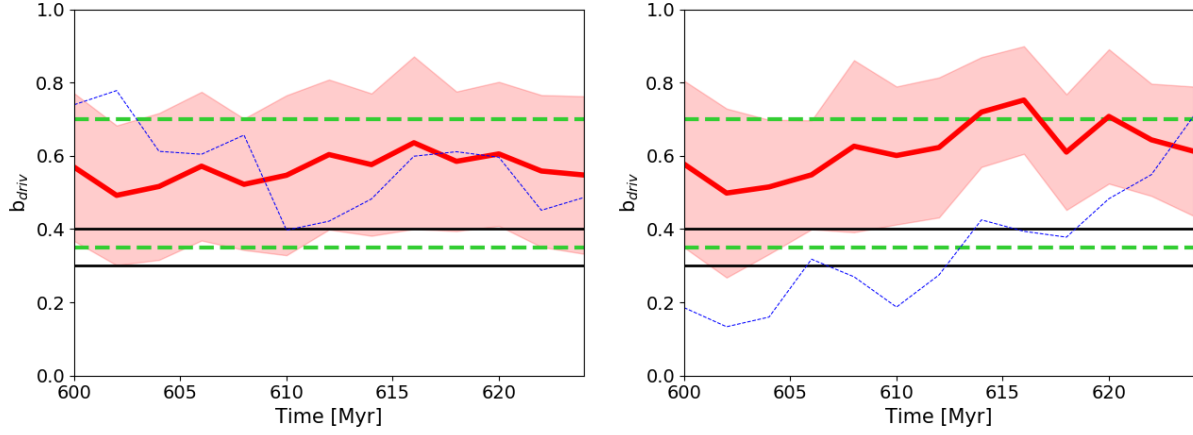


Figure 10. Dependence of the driving parameter b on changing the density threshold for defining clouds in the simulated galaxies. Evolution of identified clouds at late times in the magnetised disc. The left panel shows clouds with a minimum density of $n_{\min} = 100 \text{ cm}^{-3}$, while the right shows clouds with $n_{\min} = 10^3 \text{ cm}^{-3}$. As expected, the clouds with the higher threshold density show a slightly more compressive driving parameter, since these are more gravitationally bound/contracting. This is in agreement with Orkisz et al. (2017), who find a smaller solenoidal fraction on smaller scales. However, the time averages differ only little with $b_{\text{cloud}} \pm \Delta b_{\text{cloud}} = 0.56 \pm 0.04$ and $b_{\text{dense}} \pm \Delta b_{\text{dense}} = 0.62 \pm 0.07$.

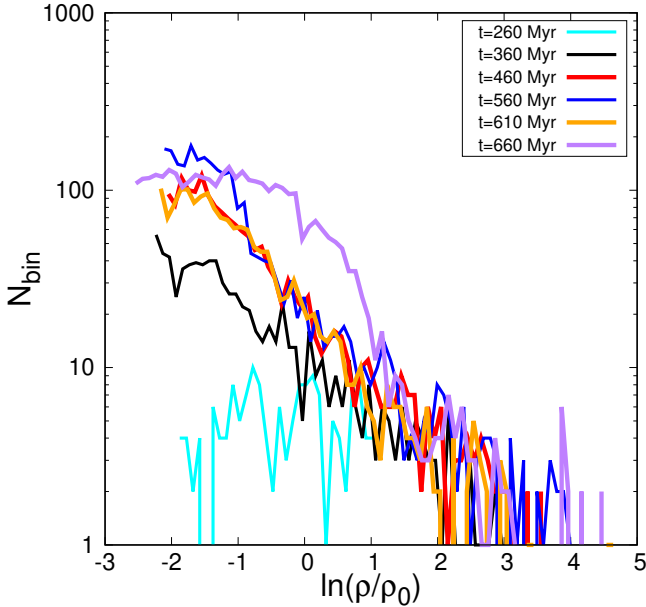


Figure A1. Probability distribution function (PDF) of the logarithmic density contrast for the example cloud at different times. The PDF is initially flat, because the cloud has just condensed out of the diffuse gas and has not developed any substructure, yet. With time, the PDF is transformed into a mixture of a log-normal and a power-law part. However, the power-law part dominates the PDF at most times, which is attributed to the rather coarse numerical resolution, which does not allow the cloud to fragment any further.

to fluctuate slightly more, but the very good agreement of the averages is convincing. Our explanation for this good correspondence is that we derive the driving parameter via the compressive ratio $\chi = \langle v_{\text{comp}}^2 \rangle / \langle v_{\text{sol}}^2 \rangle$, where resolution effects nearly cancel out.

APPENDIX C: NOTES ON THE FOURIER DECOMPOSITION

The extracted clouds in our simulations resemble regions with non-periodic boundary conditions. This can lead to significant errors in the resulting spectra due to aliasing effects. In such case, one commonly applies a window function, which enforces the field of interest to go smoothly to zero so that the box can be thought of as being periodic. The result of this *windowing* is shown in Fig. C1. The modifications to the final driving parameter are only minor. This is due to the fact that it is obtained from the compressive ratio. Thus, possible errors will cancel out as they appear in both of the decomposed fields.

DATA AVAILABILITY

The data underlying this article will be shared on reasonable request to the corresponding author.

REFERENCES

- Ballesteros-Paredes J., Hartmann L. W., Vázquez-Semadeni E., Heitsch F., Zamora-Avilés M. A., 2011, *MNRAS*, 411, 65
- Berger M. J., Olinger J., 1984, *Journal of Computational Physics*, 53, 484
- Blitz L., Fukui Y., Kawamura A., Leroy A., Mizuno N., Rosolowsky E., 2007, *Protostars and Planets V*, pp 81–96
- Bouchut F., Klingenberg C., Waagan K., 2009, *Numerische Mathematik*
- Burkhart B., Stalpes K., Collins D. C., 2017, *ApJ*, 834, L1
- Dedner A., Kemm F., Kröner D., Munz C. D., Schnitzer T., Wesenberg M., 2002, *Journal of Computational Physics*, 175, 645
- Dobbs C. L., Krumholz M. R., Ballesteros-Paredes J., Bolatto A. D., Fukui Y., Heyer M., Low M.-M. M., Ostriker

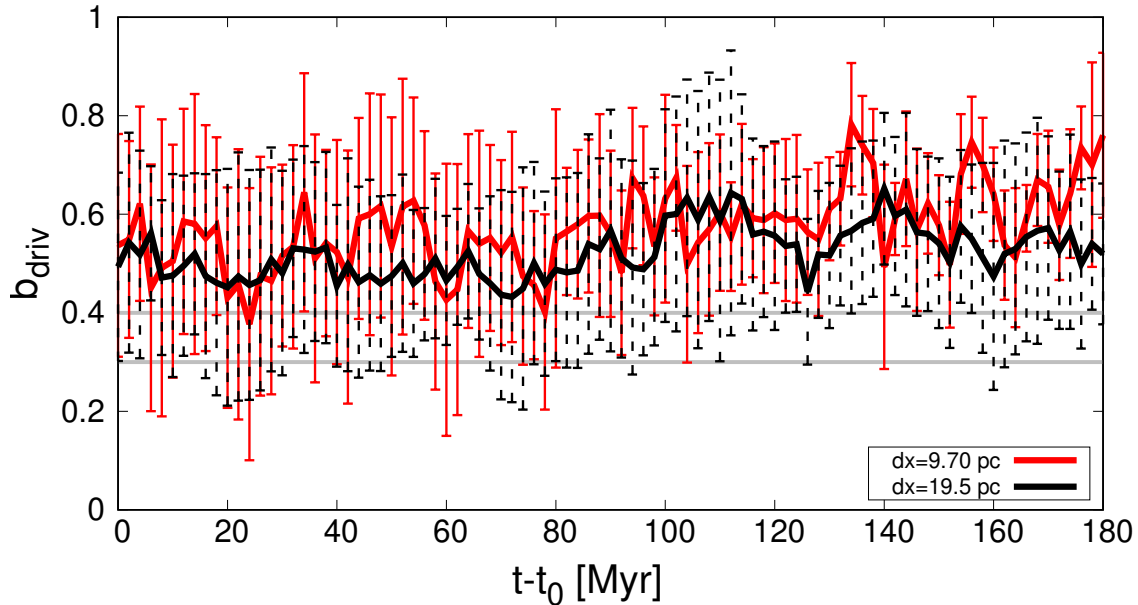


Figure B1. Resolution study of the evolution of the turbulence driving parameter for a period of 180 Myr starting at the identification of clouds (t_0). The error bars provide the standard deviation Δb_{driv} . For the two resolutions, the driving parameter obtained from the Helmholtz decomposition appears to be largely converged. The grey horizontal lines denote purely solenoidal as well as natural driving.

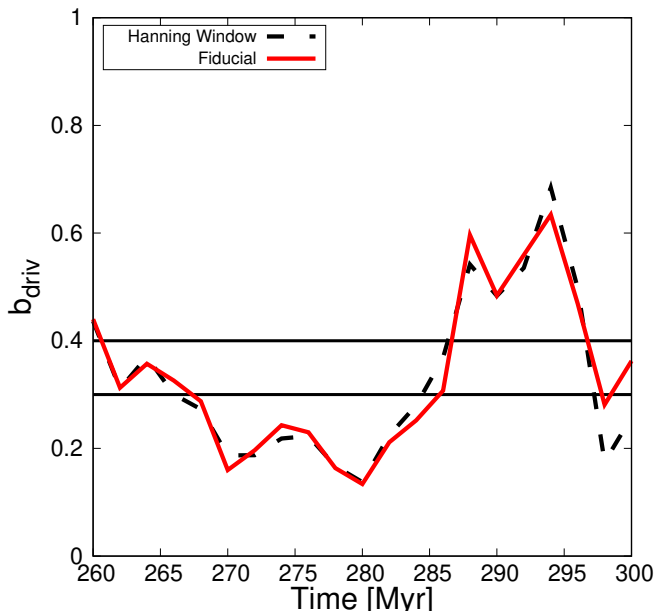


Figure C1. Comparison of the resulting driving parameter for the early phase of evolution of the example cloud. The lines show the fiducial method (red) and the result after applying a Hanning window to the turbulent velocity field. The agreement of the two methods ensures that no numerical errors emerge from e.g. aliasing effects.

E. C., Vázquez-Semadeni E., 2014, *Protostars and Planets VI*, pp 3–26

Dubey A., Fisher R., Graziani C., Jordan IV G. C., Lamb D. Q., Reid L. B., Rich P., Sheeler D., Townsley D., Weide K., 2008, in Pogorelov N. V., Audit E., Zank G. P., eds, *Numerical Modeling of Space Plasma Flows Vol. 385 of Astronomical Society of the Pacific Conference Series, Challenges of Extreme Computing using the FLASH code.*

pp 145–+

Elmegreen B. G., Scalo J., 2004, *ARA&A*, 42, 211

Federrath C., Klessen R. S., 2012, *ApJ*, 761, 156

Federrath C., Klessen R. S., 2013, *ApJ*, 763, 51

Federrath C., Klessen R. S., Schmidt W., 2008, *ApJ*, 688, L79

Federrath C., Rathborne J. M., Longmore S. N., Kruijssen J. M. D., Bally J., Contreras Y., Crocker R. M., Garay G., Jackson J. M., Testi L., Walsh A. J., 2016, *ApJ*, 832, 143

Federrath C., Rathborne J. M., Longmore S. N., Kruijssen J. M. D., Bally J., Contreras Y., Crocker R. M., Garay G., Jackson J. M., Testi L., Walsh A. J., 2017, in Crocker R. M., Longmore S. N., Bicknell G. V., eds, *IAU Symposium Vol. 322 of IAU Symposium, The link between solenoidal turbulence and slow star formation in G0.253+0.016*, pp 123–128

Federrath C., Roman-Duval J., Klessen R. S., Schmidt W., Mac Low M.-M., 2010, *A&A*, 512, A81

Federrath C., Sur S., Schleicher D. R. G., Banerjee R., Klessen R. S., 2011, *ApJ*, 731, 62

Ginsburg A., Federrath C., Darling J., 2013, *ApJ*, 779, 50

Hennebelle P., Chabrier G., 2011, *ApJ*, 743, L29

Jin K., Salim D. M., Federrath C., Tasker E. J., Habe A., Kainulainen J. T., 2017, *MNRAS*, 469, 383

Jog C. J., 2013, *MNRAS*, 434, L56

Kainulainen J., Beuther H., Henning T., Plume R., 2009, *A&A*, 508, L35

Kainulainen J., Federrath C., 2017, *A&A*, 608, L3

Konstantin L., Schmidt W., Girichidis P., Peters T., Shetty R., Klessen R. S., 2016, *MNRAS*, 460, 4483

Körtgen B., Banerjee R., Pudritz R. E., Schmidt W., 2018, *MNRAS*, 479, L40

Körtgen B., Banerjee R., Pudritz R. E., Schmidt W., 2019, *MNRAS*, 489, 5004

Körtgen B., Federrath C., Banerjee R., 2017, *MNRAS*, 472,

- 2496
- Koyama H., Inutsuka S.-i., 2002, *ApJ*, 564, L97
- Kritsuk A. G., Norman M. L., Wagner R., 2011, *ApJ*, 727, L20
- Krumholz M. R., McKee C. F., 2005, *ApJ*, 630, 250
- Larson R. B., 1981, *MNRAS*, 194, 809
- Lukat G., Banerjee R., 2016, *New A*, 45, 14
- Mac Low M.-M., Klessen R. S., 2004, *Reviews of Modern Physics*, 76, 125
- Mandal A., Federrath C., Körtgen B., 2020, *MNRAS*, 493, 3098
- Menon S. H., Federrath C., Kuiper R., 2020, *MNRAS*
- Molina F. Z., Glover S. C. O., Federrath C., Klessen R. S., 2012, *MNRAS*, 423, 2680
- Mouschovias T. C., Kunz M. W., Christie D. A., 2009, *MNRAS*, 397, 14
- Orkisz J. H., Pety J., Gerin M., Bron E., Guzmán V. V., Bardeau S., Goicoechea J. R., Gratier P., Le Petit F., Levrier F., Liszt H., Öberg K., Peretto N., Roueff E., Sievers A., Tremblin P., 2017, *A&A*, 599, A99
- Padoan P., Nordlund Å., 2011, *ApJ*, 730, 40
- Pan L., Padoan P., Haugbølle T., Nordlund Å., 2016, *ApJ*, 825, 30
- Passot T., Vázquez-Semadeni E., 1998, *Phys. Rev. E*, 58, 4501
- Scalo J., Elmegreen B. G., 2004, *ARA&A*, 42, 275
- Schneider N., Ossenkopf V., Csengeri T., Klessen R. S., Federrath C., Tremblin P., Girichidis P., Bontemps S., André P., 2015, *A&A*, 575, A79
- Seifried D., Schmidt W., Niemeyer J. C., 2011, *A&A*, 526, A14
- Tasker E. J., Tan J. C., 2009, *ApJ*, 700, 358
- Tremblin P., Schneider N., Minier V., Didelon P., Hill T., Anderson L. D., Motte F., Zavagno A., André P., Arzoumanian D., Audit E., et al., 2014, *A&A*, 564, A106
- Truelove J. K., Klein R. I., McKee C. F., Holliman J. H., Howell L. H., Greenough J. A., 1997, *ApJ*, 489, L179+
- Vázquez-Semadeni E., 1994, *ApJ*, 423, 681
- Vázquez-Semadeni E., Gómez G. C., Jappsen A. K., Ballesteros-Paredes J., González R. F., Klessen R. S., 2007, *ApJ*, 657, 870
- Völschow M., Banerjee R., Körtgen B., 2017, *A&A*, 605, A97
- Waagan K., Federrath C., Klingenberg C., 2011, *Journal of Computational Physics*, 230, 3331
- Zamora-Avilés M., Vázquez-Semadeni E., Colín P., 2012, *ApJ*, 751, 77